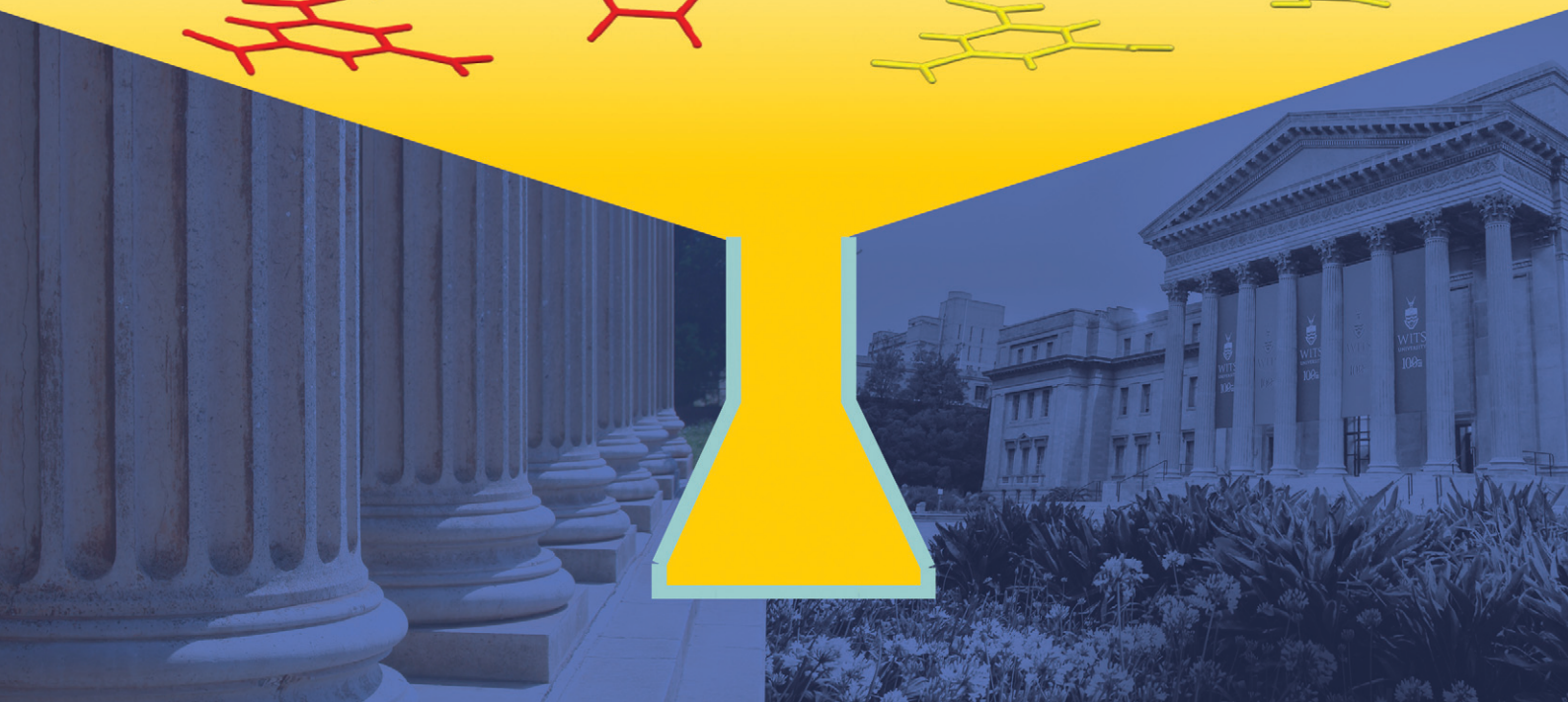
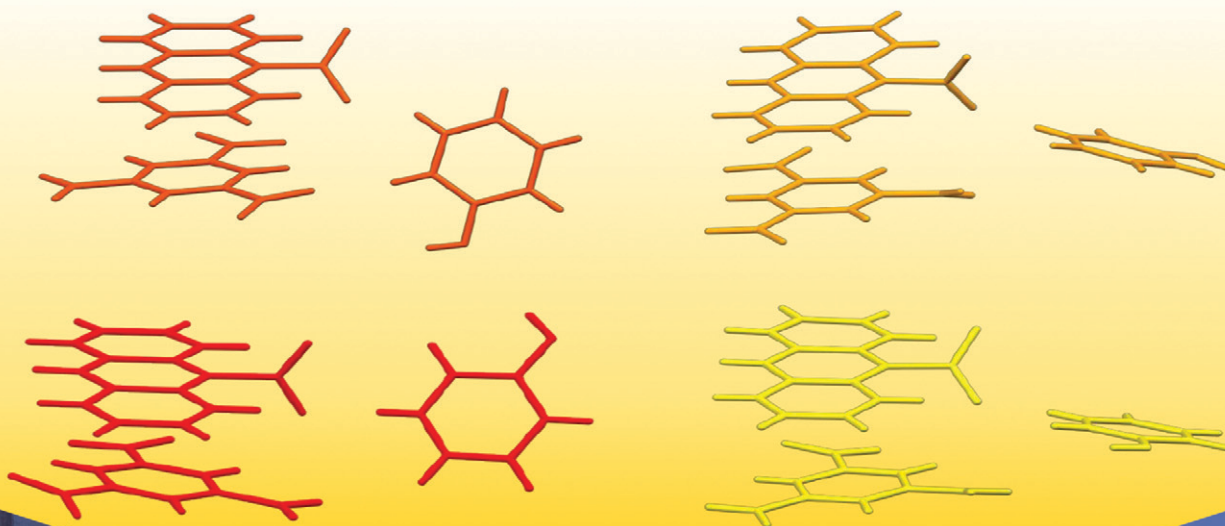


CrystEngComm

rsc.li/crystengcomm



ISSN 1466-8033

PAPER

Andreas Lemmerer *et al.*

Experimental and theoretical investigations of the optical and photoluminescence behaviour of a tetramorphic ternary molecular salt cocrystal - a quantum crystallography perspective



Cite this: *CrystEngComm*, 2025, 27, 5971

Experimental and theoretical investigations of the optical and photoluminescence behaviour of a tetramorphic ternary molecular salt cocrystal – a quantum crystallography perspective†

Atiyah Salajee,^a Anna Krawczuk,^{id}*^b Rudolph Erasmus,^{id}^c and Andreas Lemmerer,^{id}*^a

Four polymorphs of the ternary molecular salt cocrystal complex (3-hydroxypyridinium)-(9-anthracenecarboxylate)-(trinitrobenzene) were isolated. In all four polymorphs proton transfer occurred from the carboxylic acid to the nitrogen atom of the pyridine ring to form ternary molecular salts. Form I crystallizes as orange needles/rods, form II crystallizes as red blocks, and forms III and IV both crystallize as orange-yellow needles. Differential scanning calorimetry indicates that form II is the thermodynamically most stable form, further supported by energy lattices calculated within periodic boundary conditions. Quantum theory of atoms in molecules (QTAIM) analysis revealed strong hydrogen bonds and charge-transfer interactions, with notable variations in the strength of these interactions across the polymorphs. Polymorph I showed the strongest charge-assisted O–H···O hydrogen bonds, while polymorph II displayed the most significant $\pi\cdots\pi$ interactions. Photoluminescence and UV-vis studies showed that the polymorphs exhibit differing band gaps, correlating with their observed colours and electronic structures. These results emphasize the role of polymorphism in modulating the physical and chemical properties of multi-component molecular crystals.

Received 28th March 2025,
Accepted 18th July 2025

DOI: 10.1039/d5ce00338e

rsc.li/crystengcomm

Introduction

The synthesis of multi-component molecular complexes *via* cocrystallization has become increasingly popular in recent years due to the ability of cocrystallization to enhance the physiochemical properties of the starting molecular components. Cocrystal formation is dependent on the assembly of the starting molecular components through non-covalent interactions such as hydrogen bonding,^{1–3} halogen bonding,^{1,4,5} and charge-transfer (CT) interactions,^{6,7} to form a single crystal lattice.⁸ In this manner, high order cocrystals like ternary (three-component)^{1,9,10} and quaternary (four-component)^{11,12} cocrystals have been successfully synthesized. In this work ternary complexes were synthesized using 1,3,5-trinitrobenzene (**tnb**), 9-anthracenecarboxylic acid (**9-aca**), and

3-hydroxypyridine (**3hp**) as the starting components. Even though they start off as neutral components, in solution a proton transfer takes place from **9-aca** to **3hp** since ΔpK_a is 1.3, while **tnb** remains neutral. In the literature, these have been described as molecular salt cocrystals or cocrystals of salts.¹³ This situation is not as common as a pure cocrystal (only neutral components) or a pure molecular salt (all components are ionized). Our molecular salt cocrystal represents an intermediate case. A mixture of hydrogen bonding and charge transfer interactions was employed to combine the starting components to form the ternary complex. Just as for single component molecular crystals, multi-component complexes have the potential to crystallize in more than one form, known as polymorphism. Polymorphs are distinct crystal structures of the same material which arise due to the possibility of at least two different arrangements of molecules of the complex in the solid state. As a result of the differing crystal structures of polymorphic forms of a complex, polymorphs will vary in their physical and chemical properties, such as colour, melting point, crystal packing, thermodynamic stability, solubility, reactivity, *etc.* The existence of polymorphism was discovered in the early 1820's by Mitscherlich for inorganic arsenate and phosphate salt compounds and then by Wöhler and Liebig in 1832 for the organic compound benzamide.^{14–16} Since then, the study of

^aJan Boeyens Structural Chemistry Laboratory, Molecular Sciences Institute, School of Chemistry, University of the Witwatersrand, Private Bag 3, PO Wits, 2050, Johannesburg, South Africa. E-mail: andreas.lemmerer@wits.ac.za

^bInstitute of Inorganic Chemistry, University of Goettingen, Tammannstrasse 4, 37077 Goettingen, Germany. E-mail: anna.krawczuk@uni-goettingen.de

^cSchool of Physics and Materials Physics Research Institute, University of the Witwatersrand, Private Bag 3, Wits, 2050, Johannesburg, South Africa

† Electronic supplementary information (ESI) available. CCDC 2426460–2426463.

For ESI and crystallographic data in CIF or other electronic format see DOI: <https://doi.org/10.1039/d5ce00338e>



this phenomenon for single component molecular compounds has become increasingly more common and in recent years the focus has shifted to the study of polymorphism in multicomponent molecular compounds, in particular cocrystals. Numerous experiments have been conducted to synthesize cocrystals and identify novel polymorphic forms of these cocrystals. Two polymorphs each of the binary (two component) cocrystals urea:4,4'-bipyridine,¹⁷ salicylic acid:4,4'-bipyridine,¹⁷ caffeine: citric acid,¹⁸ sulfadimidine:4-aminosalicylic acid,¹⁹ caffeine: niflumic acid,²⁰ and carbamazepine: methylparaben²¹ have all been reported. Sangtani and co-workers investigated cocrystals of furosemide with 2,2'-bipyridine, 4-aminopyridine, and 4,4'-bipyridine.²² Interestingly, two polymorphic forms of the cocrystal furosemide:4,4'-bipyridine were isolated and exhibit colour polymorphism despite the starting components both being colourless. The cocrystals of furosemide with 2,2'-bipyridine and 4-aminopyridine were both colourless and do not exhibit polymorphism. Zaworotko and co-workers isolated three polymorphic forms of the 1:1 ionic cocrystal lithium 4-methoxybenzoate:1-proline.²³ Although polymorphism is largely serendipitous, attempts to achieve different polymorphic forms include varying crystallization growth conditions and utilizing different crystallization methods/techniques.²⁴ These include but are not limited to, varying pressures and temperatures, crystallization from solution using different solvents, dry and wet grinding, and crystallization from the melt. The discovery of multiple polymorphic forms of binary (two-component) cocrystals has become common, however polymorphism screening in ternary (three-component) cocrystals is still rare. The first report of a trimorphic ternary system was by Lemmerer in 2020 where he isolated three polymorphs of the ternary molecular salt complex (2-aminopyridinium)-(9-anthracenecarboxylate)-(trinitrobenzene).²⁵ This motivated our research to focus on finding novel polymorphs of ternary molecular compounds. Four polymorphs of the ternary molecular salt cocrystal (3-hydroxypyridinium)-(9-anthracenecarboxylate)-(trinitrobenzene) were discovered and isolated. All four polymorphic forms exhibit proton transfer from the carboxylic acid to the pyridine to form ternary molecular salts. Because of the colour polymorphism,²⁶ we also investigated the optical behaviour and correlated it as best as possible to calculations done.

Experimental and analytical methods

Experimental setup

All reagents used for synthesis and characterization were of analytical grade, purchased from Sigma-Aldrich, unless otherwise stated. Reagents were used as received, without further purification. In most experiments, a 1:1:1 stoichiometric ratio was used. 20 mg of trinitrobenzene, 20 mg of 9-anthracenecarboxylic acid and 9 mg of 3-hydroxypyridine were weighed out. In some experiments,

the amount of pyridine used was increased, giving a stoichiometric ratio of 1:1:3 of **tnb**:**9aca**:**3hp**. Ethanol, methanol, acetonitrile, ethyl acetate and tetrahydrofuran were used as solvents. All solutions were heated and stirred to achieve complete dissolution.

Vapour diffusion

Stoichiometric amounts of the starting components were weighed out into glass vials. A solvent was added to the vial. This was then placed into a larger glass vial containing the anti-solvent, hexane. Form **I** crystallised out when ethanol was used as the solvent and form **IV** crystallised out when methanol was used.

Zone refinement crystallization

An Optical Heating and Crystallization Device (OHCD) was employed to facilitate *in situ* cocrystallization of the ternary molecular system. Firstly, stoichiometric amounts of the starting components were weighed out into a glass vial, which was then placed on a Kofler hot bench and allowed to melt. The melt was sucked up into a capillary. The capillary was sealed and mounted into a Bruker Venture D8 Photon CMOS diffractometer fitted with an OHCD. Form **I** was obtained.

Single crystal X-ray diffraction (SCXRD)

All data collections were obtained on a Bruker Venture D8 Photon CMOS diffractometer with graphite-monochromated MoK α_1 ($\lambda = 0.71073 \text{ \AA}$) radiation at 173 K using an Oxford Cryostream Plus cooler. The collection method involved ω -scans with a 0.5° width. SAINT+ version 6.0 (ref. 27) software was used for data reduction and SADABS²⁸ was used to make empirical absorption corrections. The crystal structures were solved using direct methods on SHELXS-2018.²⁹ Non-hydrogen atoms were first refined isotropically, followed by anisotropic refinement by full matrix least-squares calculations based on F^2 using SHELXL-2018.²⁹ Details of the treatment of H atoms involved in hydrogen bonding are given in the ESI,[†] as well as the positional disorder of the **tnb** in form **II**. Diagrams and publication material were generated using WinGX,³⁰ ORTEP-3,³⁰ PLATON³¹ and MERCURY.³²

Powder X-ray diffraction (PXRD)

Powder X-ray diffraction data patterns were collected at 293 K on a Bruker D2 Phaser diffractometer which employed a sealed tube Co X-ray source ($\lambda = 1.78897 \text{ \AA}$), operating at 30 kV and 10 mA, and LynxEye PSD detector in Bragg-Brentano geometry. The calculated powder diffraction patterns were computed from the single crystal data which was collected at 173 K using Mercury. The peak positions are shifted resulting from the different temperatures at which the samples were measured. The peak intensities vary due to preferred orientation.



Differential scanning calorimetry (DSC)

Differential scanning calorimetry data (Tables S12–S15†) were collected using a Mettler Toledo DSC3 with aluminium pans under N₂ gas purge (10 mL min⁻¹). Star SW 16.20 was used for instrument control and data analysis. Exothermic events were shown as peaks. The temperature and energy calibrations were performed using pure indium (purity 99.99%, m.p. 156.6 °C, heat of fusion 28.45 J g⁻¹) and pure zinc (purity 99.99%, m.p. 419.5 °C, heat of fusion 112 J g⁻¹).

Fourier transform infrared spectroscopy (FTIR)

FTIR spectra of the samples were collected using a Bruker Alpha II, fitted with an ATR eco ZnSe crystal, with a spectral range of 20 000–500 cm⁻¹. OPUS software, version 8.5, was used to analyse and characterize the spectra.

Photoluminescence spectroscopy (PL)

Solid-state photoluminescence spectra of powder samples of forms **I**, **II**, **III** and **IV** were acquired at room temperature using a Horiba QuantaMaster 8000 spectrofluorometer with a Xe lamp and a Horiba PPD-850 detector. Emission correction was applied to the reported data.

Diffuse reflectance spectroscopy (DRS)

Diffuse reflectance spectra of all four polymorphs in the UV-vis spectral range were acquired at room temperature using a Varian Cary 500 UV-vis-NIR spectrophotometer equipped with a Harrick Scientific Product Praying Mantis™ Diffuse Reflection Accessory.

Computational details

Crystal lattice energies and band structure

Crystal lattice energies and band structures of the studied polymorphs were calculated using CRYSTAL23 software package.³³ Crystal structures were optimized in constrained experimental unit cells of the studied compounds, to ensure the crystals were their equilibrium crystal structure. In case of polymorph **II**, the disorder resulting from trinitrobenzene (**tnb**) lying on a center of inversion and occupying two different orientations, was removed by lowering the symmetry of the crystal structure from *P* $\bar{1}$ to *P*1. For more details, the reader is referred to ESI† Geometry optimization and further calculations were performed using PBE0 hybrid functional combined with the pob-DZVP basis set³⁴ and including the Grimme D3 dispersion correction.³⁵ A mesh of 5 × 5 × 5 *k*-points in reciprocal space was generated according to the Monkhorst–Pack method³⁶ and the condition for the self-consistent field (SCF) was set to 10⁻¹⁰ on the total energy difference between two subsequent cycles. For the calculations of lattice energies, the wavefunction of the isolated molecules in crystal geometry were also computed. The basis set superposition error (BSSE) was corrected by the counterpoise approach.³⁷ To further obtain electronic band structures and density of state (DoS) of the polymorphs, the

band path on which *k*-vectors were sampled in reciprocal space was chosen by defining irreducible Brillouin zone, which coincides with Bravais lattice of the studied compound. The strategy was selected based on the findings presented in the manuscript by Hinuma and colleagues.³⁸ Additionally, density of states (DOS) for each polymorph was projected on all atomic orbitals.

Intermolecular interactions

The nature of intermolecular interaction, in particular π - π interactions and hydrogen bond of N–H \cdots O and O–H \cdots O type, was examined through the use of periodic and gas-phase calculations. Single-point DFT calculations were conducted with the use of Gaussian16 (ref. 39) at the same level of theory as that employed for lattice energies and electron density estimation. The geometries used for modelling were taken from the periodic DFT-optimized crystal structures described in the Crystal lattice energies and band structure section. As these optimizations were carried out within the experimental unit cell constraints, all subtle structural differences associated with polymorphism were preserved. No additional preoptimization of molecular fragments was performed. For gas-phase calculations, asymmetric units containing the relevant intermolecular interactions were directly extracted from these optimized structures. Calculations were done with the use of Gaussian16 software.³⁹ Counterpoise correction was included using scheme proposed by Boys and Bernardi³⁷ to correctly account for BSSE error. More details are given in ESI† file. The wave functions obtained were subsequently employed in a quantitative NCI (non-covalent interactions) analysis, whereby reduced density gradients (RDGs) were generated and electron density properties were calculated within the RDG regions. All NCI-related calculations were conducted using NCIPLOT software.⁴⁰ Further details on NCI analysis is given in ESI† file in section J. Computational details.

Results and discussion

The four polymorphs were isolated at room temperature (Fig. 1) and their structures determined using single crystal X-ray diffraction. Crystallographic data, powder X-ray diffraction patterns and infrared spectra of the four polymorphs are given in the ESI† In addition to solvent evaporation and vapour diffusion cocrystallization experiments, an Optical Heating and Crystallization Device (OHCD) was also employed to facilitate *in situ* cocrystallization of the ternary molecular system. This device allows the crystallization process to occur inside a glass capillary, mounted *in situ* in the diffractometer, under the flow of nitrogen gas. A CO₂ gas laser is used to heat the capillary. The laser is moved from the bottom of the capillary to the top which results in moving molten zones wherein recrystallization will take place as the laser is moved upwards. This repetitive heating–cooling process (zone refinement) leads to the formation of a single crystal in the



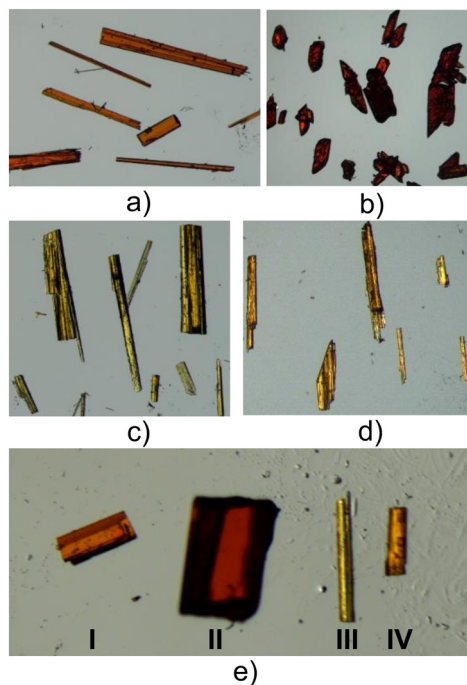


Fig. 1 Crystal images of (a) form I, (b) form II, (c) form III, (d) form IV, and (e) forms I, II, III, and IV.

capillary (Fig. S1†). In this manner form I was also successfully obtained (Fig. S2†).

Form I crystallizes as orange needles/rods in the space group $P2_1/c$, form II crystallizes as red blocks in the space group $P\bar{1}$, form III crystallizes as orange-yellow needles in the space group $P2_1/c$, and form IV crystallizes as orange-yellow needles in the space group $P2_1/n$ (Fig. 1). The asymmetric units of the four polymorphs each contain one molecule/ion each of the three starting components (Fig. 2). Interestingly, the **tnb** molecule in form II appears as two overlapping molecules in the asymmetric unit (Fig. S3†), however it is a single molecule of **tnb** that lies on a center of inversion and can therefore occupy two different orientations. In all four polymorphs, **tnb** acts as the acceptor in a $\pi \cdots \pi$ charge transfer (CT) interaction with the aromatic system of **9aca**⁽⁻⁾. The **3hp**⁽⁺⁾ cation is bonded to the **9aca**⁽⁻⁾ anion, in all four polymorphs, through a charge-assisted $N^{(+)}-H \cdots O^{(-)}$ hydrogen bond (HB) from the pyridinium cation to the carboxylate and through a second charge-assisted $O-H \cdots O^{(-)}$ hydrogen bond from the hydroxyl group of the pyridine to the carboxylate group of a neighbouring **9aca**⁽⁻⁾ anion (Fig. 3). In particular, in form II these hydrogen bonding interactions exist between neighbouring **3hp**⁽⁺⁾ cations and **9aca**⁽⁻⁾ anions to form an $R_2^2(18)$ ring (Fig. 3b). In contrast,

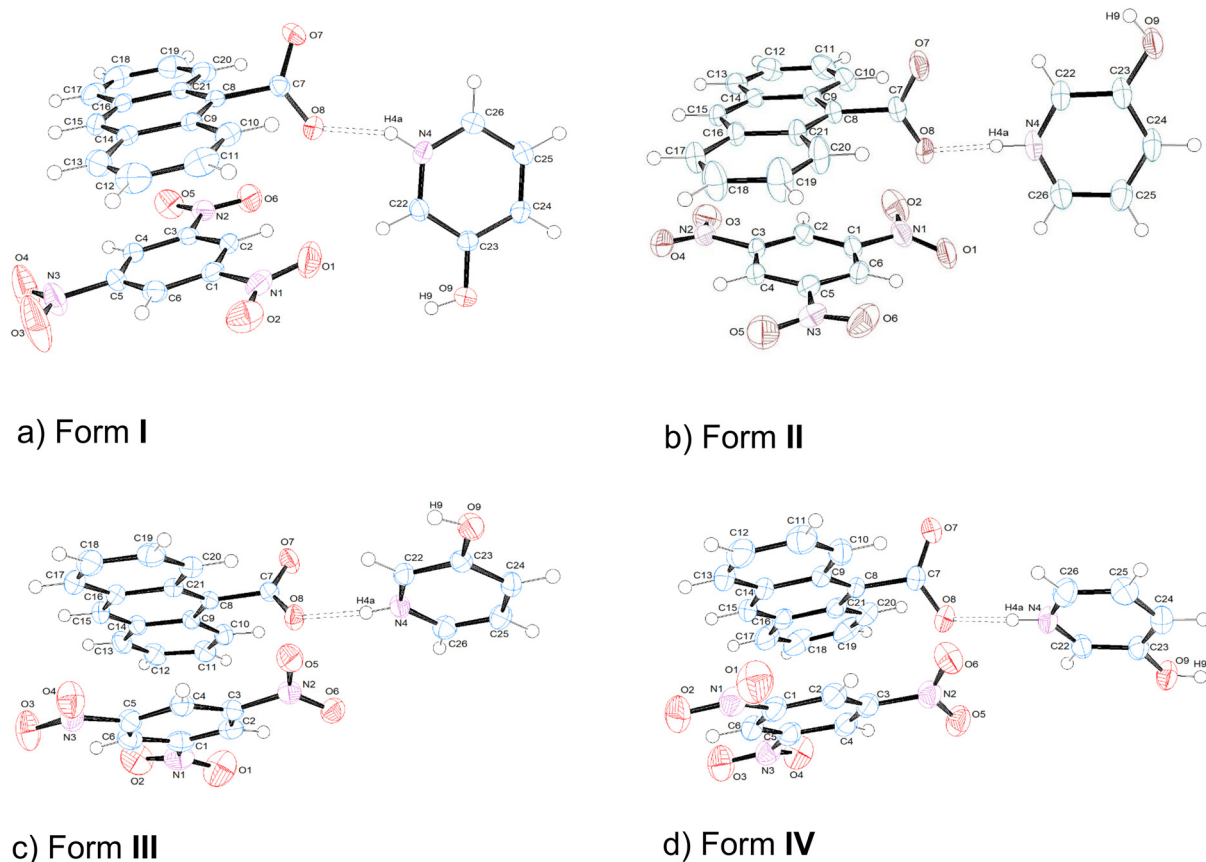


Fig. 2 Asymmetric unit of (a) form I, (b) form II, (c) form III, and (d) form IV indicating the numbering scheme, ellipsoids at 50% probability. Symmetry-independent hydrogen bonding interactions are shown as a dashed bond.



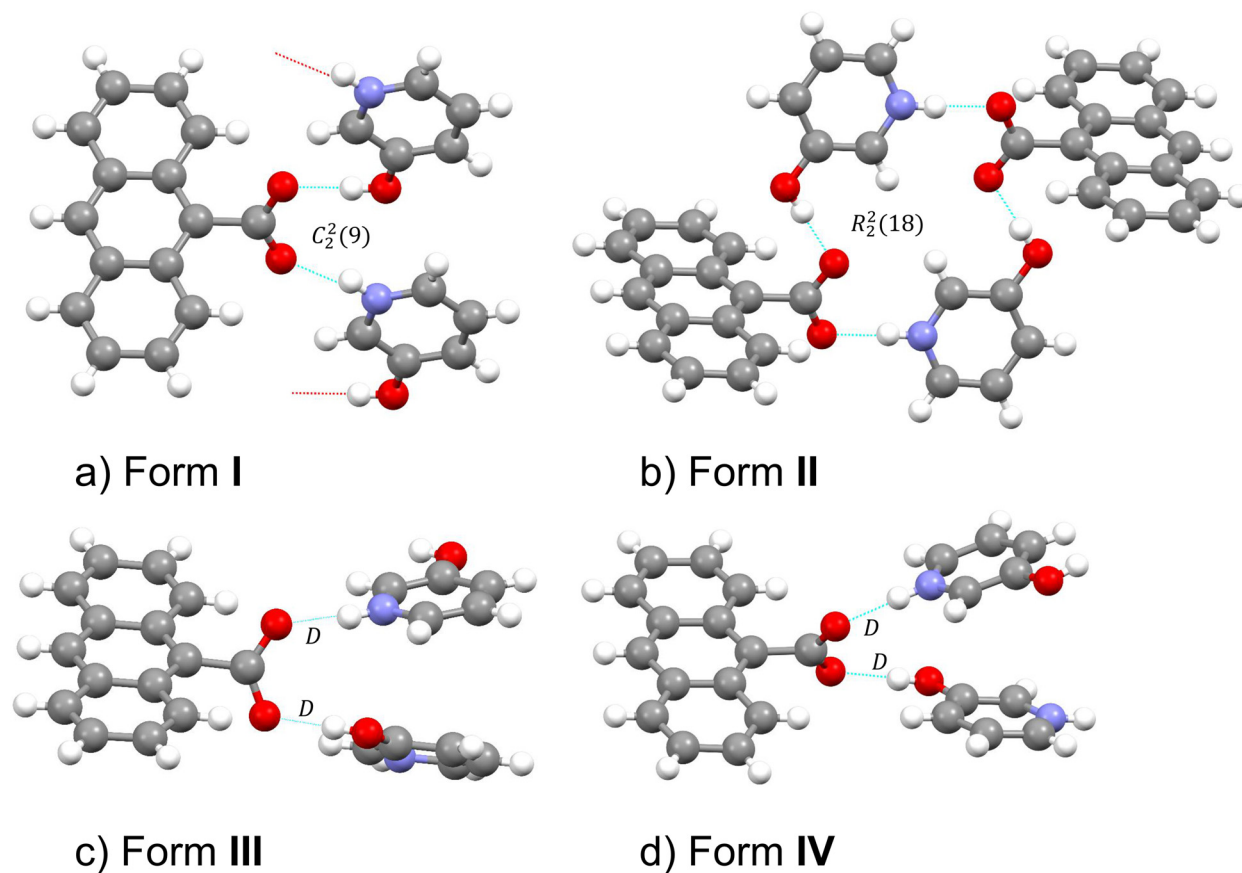


Fig. 3 The hydrogen bonding interactions in the four forms, showing the graph set notations.

in form **I**, these hydrogen bonding interactions between the **9aca**⁽⁻⁾ anion and two neighbouring **3hp**⁽⁺⁾ cations form a $C_2^2(9)$ chain, while in forms **III** and **IV**, they form discrete D and D motifs (Fig. 3a, c and d).⁴¹ The conformation the carboxylate group makes is due to an anion $\cdots\pi$ -hole contact which exists between one carboxylate oxygen atom (O8) and one nitrogen atom (N2). The distances of these short contacts are 2.78(1), 2.79(1) and 2.80(1) Å respectively for forms **II**, **III** and **IV** (Fig. S4[†]). A UNI force field in the MERCURY^{42,43} package was used to make simplified qualitative comparisons of the intermolecular potentials in the four polymorphs. The strongest interactions are the CT interactions. In form **I**, **tnb** has intermolecular potentials of -65.2 and -61.1 kJ mol⁻¹ respectively with the neighbouring two **9aca**⁽⁻⁾ anions on either side of **tnb** (Fig. S5[†]). The next strongest interaction in form **I** is the charge-assisted O–H \cdots O⁽⁻⁾ hydrogen bond from the hydroxyl group of the pyridine to the carboxylate of the **9aca**⁽⁻⁾ anion at -20.7 kJ mol⁻¹, followed by the N⁽⁺⁾–H \cdots O⁽⁻⁾ hydrogen bond from the pyridinium cation to the carboxylate of the **9aca**⁽⁻⁾ anion at -11.3 kJ mol⁻¹. In form **II**, **tnb** has intermolecular potentials of -113.9 and -113.3 kJ mol⁻¹ respectively with neighbouring **9aca**⁽⁻⁾ anions on either side of **tnb** (Fig. S5[†]). The next strongest interaction in form **II** is the charge-assisted O–H \cdots O⁽⁻⁾ hydrogen bond from the hydroxyl group of the pyridine to the carboxylate at -27.4 kJ mol⁻¹, followed by the N⁽⁺⁾–H \cdots O⁽⁻⁾ hydrogen bond from the

pyridinium cation to the carboxylate at -16.0 kJ mol⁻¹. In form **III**, **tnb** has intermolecular potentials of -57.0 and -49.4 kJ mol⁻¹ respectively with the neighbouring two **9aca**⁽⁻⁾ anions on either side of **tnb** (Fig. S5[†]). The next strongest interaction in form **III** is the charge-assisted O–H \cdots O⁽⁻⁾ hydrogen bond from the hydroxyl group of the pyridine to the carboxylate at -23.9 kJ mol⁻¹, followed by the N⁽⁺⁾–H \cdots O⁽⁻⁾ hydrogen bond from the pyridinium cation to the carboxylate at -20.2 kJ mol⁻¹. In form **IV**, **tnb** has intermolecular potentials of -61.0 and -57.8 kJ mol⁻¹ respectively with the neighbouring two **9aca**⁽⁻⁾ anions on either side of **tnb** (Fig. S5[†]). The next strongest interaction in form **IV** is the charge-assisted O–H \cdots O⁽⁻⁾ hydrogen bond from the hydroxyl group of the pyridine to the carboxylate at -26.1 kJ mol⁻¹, followed by the N⁽⁺⁾–H \cdots O⁽⁻⁾ hydrogen bond from the pyridinium cation to the carboxylate at -20.4 kJ mol⁻¹.

As previously stated, the UNI approach offers a qualitative rather than a quantitative assessment of the bonding situation in a studied system. Therefore, to gain further insight into intermolecular interactions in the polymorphs and to more accurately quantify the strength of those interactions, we conducted a full topological analysis of theoretically-derived electron density, using the quantum theory of atoms in molecules (QTAIM),⁴⁴ one of the tools commonly employed in the field of quantum crystallography



Table 1 Topological analysis of theoretically derived electron density in the region of intermolecular interactions of O–H...O⁽⁻⁾ and N⁽⁺⁾–H...O⁽⁻⁾, at the bond critical points (BCPs). All values refer to calculations performed in boundary conditions using crystal orbitals approach. $\rho(\mathbf{r})/e \text{ \AA}^{-3}$, $\nabla^2\rho(\mathbf{r})/e \text{ \AA}^{-5}$, $G(\mathbf{r}_{\text{CP}})$ and $V(\mathbf{r}_{\text{CP}})$ are local kinetic and local potential energy density ($e \text{ \AA}^{-3}$), respectively, $E(\mathbf{r}_{\text{CP}})$ is electronic local energy density ($e \text{ \AA}^{-3}$). Abramov's expression⁴⁷ was used to obtain local kinetic and potential energy densities

	$\rho(\mathbf{r})$	$\nabla^2\rho(\mathbf{r})$	$G(\mathbf{r}_{\text{CP}})$	$V(\mathbf{r}_{\text{CP}})$	$E(\mathbf{r}_{\text{CP}})$	$ V(\mathbf{r}_{\text{CP}}) /G(\mathbf{r}_{\text{CP}})$
O9–H9...O7						
I	0.533	4.58	0.42	-0.52	-0.10	1.23
II	0.466	4.58	0.38	-0.44	-0.06	1.17
III	0.421	4.10	0.34	-0.39	-0.05	1.15
IV	0.435	4.34	0.36	-0.41	-0.05	1.14
N4–H4A...O8						
I	0.362	4.10	0.31	-0.34	-0.02	1.08
II	0.434	4.34	0.34	-0.43	-0.03	1.39
III	0.400	4.34	0.34	-0.37	-0.03	1.10
IV	0.383	4.10	0.32	-0.35	-0.03	1.11

(QCr).^{45,46} QTAIM uniquely characterizes intermolecular interactions by analyzing the electron density (ED)

distribution to identify bond critical points (BCPs), and ED derivatives such as: Laplacian, potential and kinetic energy densities and others,^{47,48} providing a quantitative understanding of bonding, without relying on empirical parameters. Among all O–H...O⁽⁻⁾ hydrogen bonds identified in the studied polymorphs, the strongest one appears to be present in form I (see Table 1), with the density $\rho(\mathbf{r})$ at BCP being $0.533 e \text{ \AA}^{-3}$ and Laplacian $\nabla^2\rho(\mathbf{r}) = 4.58 e \text{ \AA}^{-5}$. This observation is well supported by the analysis of the noncovalent interaction (NCI) index, both the reduced density gradient (RDG) surface and the 2D plots of RDG *versus* the product of electron density and the sign of the second eigenvalue of the Hessian matrix (see Fig. 4). The RDG domain in form I is represented by a well-defined, compact, disc-shaped surface, which is colored predominantly blue, reflecting a strongly attractive interaction. This blue coloring is a consequence of the features observed in the 2D RDG plot, where the spike associated with this particular interaction shows the greatest shift toward the negative region compared to other polymorphs. This shift indicates the most attractive interaction, which corresponds to the strongest hydrogen

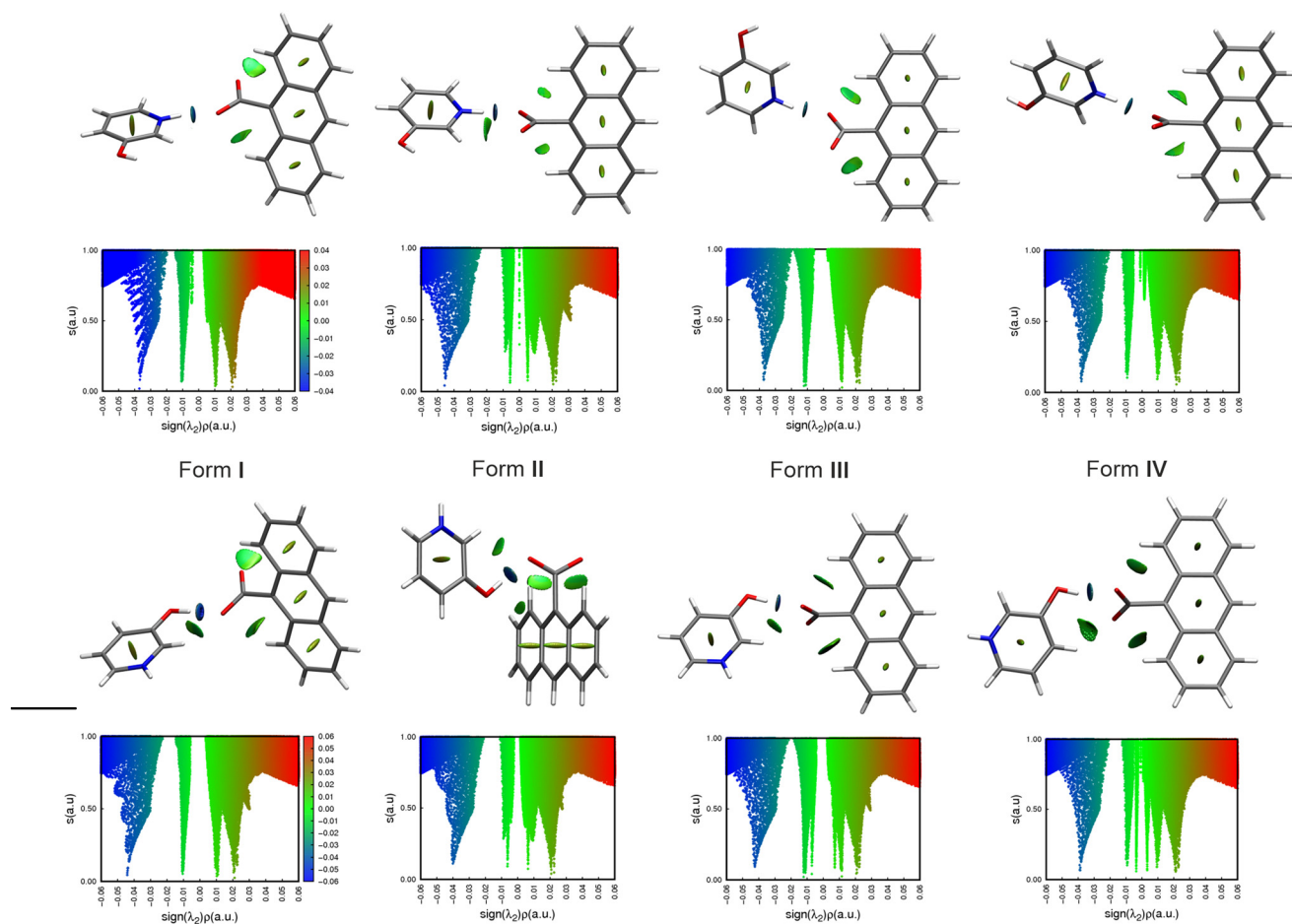


Fig. 4 Gradient isosurfaces of reduced density gradient, RDG in the area of O–H...O⁽⁻⁾ and N⁽⁺⁾–H...O⁽⁻⁾ hydrogen bonds identified in all four polymorphs supplied by fingerprint plots of the reduced density gradient (RDG) vs. the electron density multiplied by the sign of the second Hessian eigenvalue. Gradient surfaces are plotted at 0.1 au level. Full QTAIM characteristics of the bond critical points is given in Table 1.



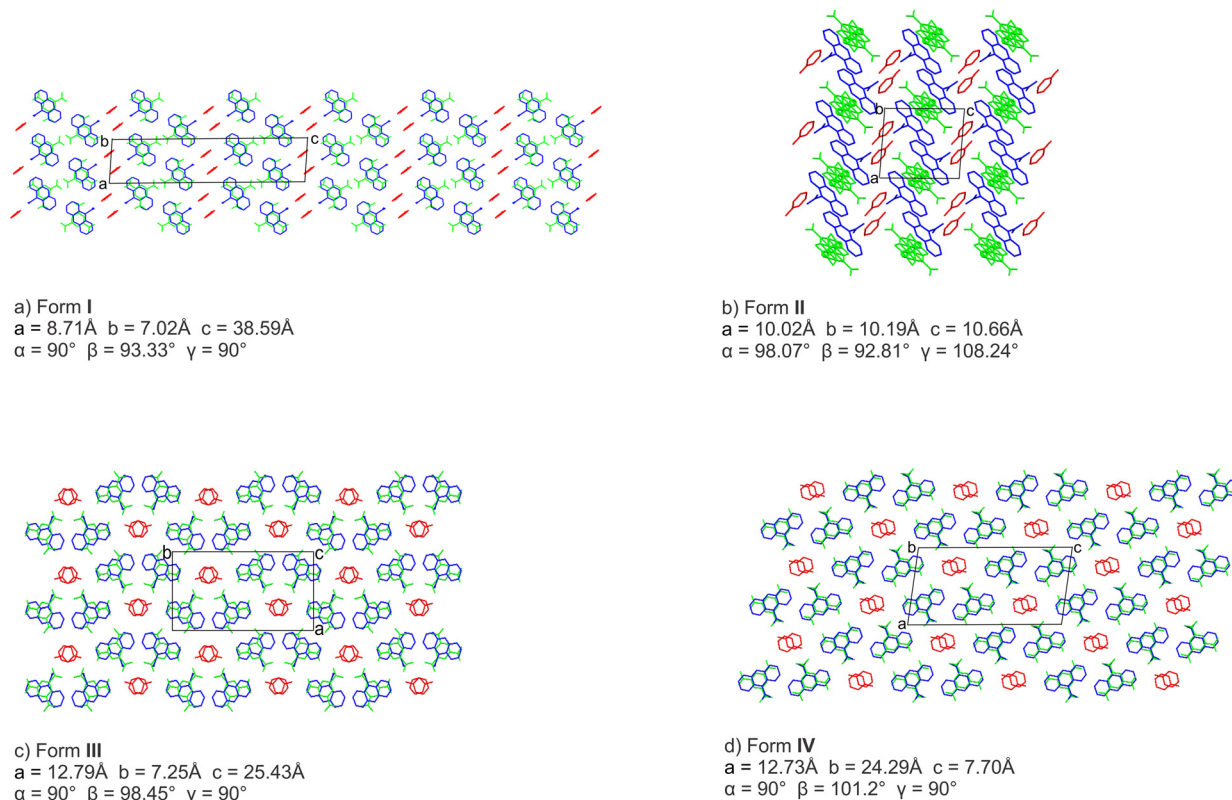


Fig. 5 The packing of the four polymorphic forms shown along with their respective unit cell parameters (green represents the **tnb** molecule, blue represents the **9aca⁻** anion, and red represents the **3hp⁺** cation).

bond of this type. In other polymorphs the electron density at a bond critical point is on average 0.426 e \AA^{-3} . This finding is at odds with the UNI force field method, which indicated that the strongest charge-assisted $\text{O-H}\cdots\text{O}^{(-)}$ interaction is present in polymorph **II**. However, it is essential to note that the assessment of intermolecular potentials considers the entire molecule, not a single chosen interaction, as in the case of QTAIM. Therefore, the contribution from other atoms may augment the overall value of the potential. A similar situation may be observed when analyzing the charge-assisted $\text{N}^{(+)}\text{-H}\cdots\text{O}^{(-)}$ hydrogen bonds. Here, QTAIM points to polymorph **II** to have the strongest interactions of this type (see Table 1 and Fig. 4), whereas the UNI approach indicates polymorph **IV**. Nonetheless, all the charge-assisted HBs are considered to be strong and of intermediate character, in accordance with the formulas proposed by Espinosa and coworkers.⁴⁹ The intermediate character between the pure closed-shell and shared interactions is indicated by the ratio between the absolute value of potential energy density and kinetic energy density, being greater than 1 but less than 2 for all the interactions. However, it is evident that $\text{O-H}\cdots\text{O}^{(-)}$ HBs possess a notably higher degree of covalent character in comparison to those of the $\text{N}^{(+)}\text{-H}\cdots\text{O}^{(-)}$ type, suggesting they have a more pronounced role in self-assembly of the studied systems.

To ensure accurate assessment of the $\pi\cdots\pi$ charge transfer interactions between the **tnb** and **9aca⁻** molecules across all

polymorphs, we recognized the limitations of the UNI force field method, which may overestimate or underestimate these interactions. Therefore, we complemented our analysis with QTAIM and calculated interaction energies for dimers extracted from the crystal structures. According to quantum chemical simulations the strength of the $\pi\cdots\pi$ interaction decreases in the following order: **III** ($-46.90 \text{ kJ mol}^{-1}$) > **II** ($-40.88 \text{ kJ mol}^{-1}$) > **IV** ($-32.34 \text{ kJ mol}^{-1}$) > **I** ($-27.82 \text{ kJ mol}^{-1}$). However, one should be cautious about drawing definitive conclusions here, since in each polymorph we observe a

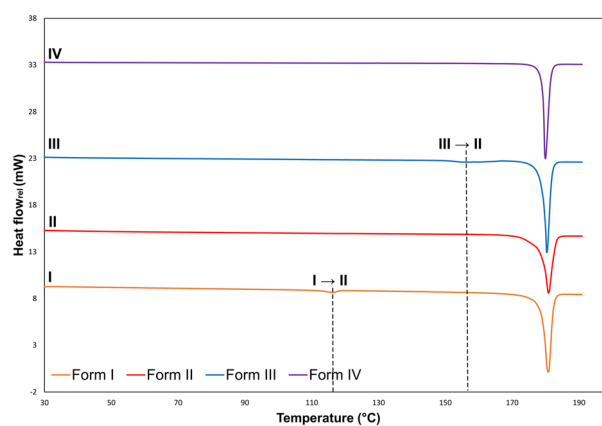


Fig. 6 Representative DSC traces of samples of forms I, II, III, and IV. Exotherms are up.



Table 2 Results of DSC experiments^a and calculated lattice energies^b

Polymorph	$T_{\text{onset}}/^{\circ}\text{C}$	$T_{\text{peak}}/^{\circ}\text{C}$	Enthalpy/ kJ mol^{-1}	Lattice energy/ kJ mol
Form I \rightarrow II	112.1 ± 0.1	116.2 ± 0.8	-1.95 ± 0.20	-859.722
Form II melting	178.6 ± 0.1	180.8 ± 0.3	-56.0 ± 2	
Form II	178.9 ± 0.7	181.0 ± 0.3	-68.5 ± 0.4	-866.54
Form III \rightarrow II	153.9 ± 0.5	159.5 ± 0.1	-4.87 ± 0.58	-865.23
Form II melting	177.9 ± 0.6	180.0 ± 0.2	-63.6 ± 0.3	
Form IV	178.9 ± 0.3	179.9 ± 0.2	-65.8 ± 0.2	-869.91

^a All values were calculated from duplicate/triplicate measurements. ^b Calculated with the use of Crystal23 software.³³

different overlap of interacting molecules, and thus a different “set” of interacting atoms (see geometrical parameters in Table S16[†]). That is particularly evident when one visualizes so called reduced density gradient (RDG) surfaces (Fig. S23[†]) calculated with the use of NCI approach.^{50,51} We do not observe well-defined small domains, characteristic for strong non-covalent interactions such as previously discussed (compare with Fig. 4) O–H \cdots O⁽⁻⁾ and N⁽⁺⁾–H \cdots O⁽⁻⁾ hydrogen bonds. Instead, we see broad, multi-shaped surfaces that indicate the presence of weak, rather van der Waals-like interactions. Each of the domains have a different shape depending how many contacts are identified as effective ones between the two molecules (see molecular graphs in Fig. S23[†]). For example, in case of polymorph III most of the contacts are identified between the carbon atoms of the **tnb** phenyl group and anthracene backbone of **9aca**⁽⁻⁾, whereas in case of polymorph I, we observe high contribution from the substituents, *i.e.* nitro groups and thus smaller overlap between aromatic moieties. That could be one of the possible explanations why the interaction energy for form III is higher than the one calculated for form I. Nonetheless, properties of electron density evaluated at BCPs (see Table S18 in the ESI[†]) for all identified contacts contributing to the π - π CT interactions, confirm the presence of weak NCIs of pure closed-shell character with more dominant attractive components, as seen on the finger plots of the RDG *vs.* the electron density $\rho(\mathbf{r})$ multiplied by the sign of the second Hessian eigenvalue, $\text{sign}(\lambda_2)$, in Fig. S23[†].

The packing of the four polymorphs, as shown in Fig. 5, highlights the significant difference in the arrangement of molecules/ions in the solid states of the four polymorphs. Form I has **3hp**⁽⁺⁾ cations in a zig-zag pattern, along the *a*-axis, in between rows of (**tnb**)-(**9aca**⁽⁻⁾) CT dimers. Form II has its **3hp**⁽⁺⁾ cations in single rows, along the *a*-axis, between **tnb** molecules and **9aca**⁽⁻⁾ anions. In form III, pairs of **3hp**⁽⁺⁾ cations form a wave-like pattern with (**tnb**)-(**9aca**⁽⁻⁾) CT

dimers along the *b*-axis, whilst in form IV the pairs of **3hp**⁽⁺⁾ cations form straight rows with the (**tnb**)-(**9aca**⁽⁻⁾) CT dimers along the *c*-axis.

Determining the melting points and enthalpies of fusions of polymorphs is an important aspect in polymorph screening since they will determine which polymorph is the most thermodynamically stable form. Differential scanning calorimetry (DSC) traces of the four polymorphs are shown in (Fig. 6). The DSC trace (orange) of form I shows a phase transition at 112.1 °C with an enthalpy of $-1.95 \text{ kJ mol}^{-1}$, and thereafter a melting endotherm at 178.6 °C (Table 2). Similarly, form III (blue DSC trace) also undergoes a phase transition, however it occurs at 153.9 °C with an enthalpy of $-4.87 \text{ kJ mol}^{-1}$, and thereafter melting at 177.9 °C. The DSC traces of forms II (red) and IV (purple) each show a single melting endotherm at 178.9 °C, with enthalpies of fusion of $-68.5 \text{ kJ mol}^{-1}$ and $-65.8 \text{ kJ mol}^{-1}$ respectively. Although the melting of forms II and IV occur at the same average temperature their enthalpies of fusion differ, with form II having the largest enthalpy value of the four forms, therefore form II is the most thermodynamically stable form. The stability of the studied polymorphs was also assessed by lattice energies obtained from periodic calculations. The highest lattice energy is observed for polymorph IV with the value of $-869.91 \text{ kJ mol}^{-1}$, whereas polymorph II is the second most stable compound, with energy of $-866.54 \text{ kJ mol}^{-1}$. Lattice energies for forms III and I, are -865.23 and $-859.722 \text{ kJ mol}^{-1}$, respectively. These disagreements with experimental results may be due to the fact that crystal lattice calculations often assume idealized conditions, such as perfect, defect-free crystal structure and static lattice. Importantly, the periodic DFT calculations used to obtain lattice energies are performed at 0 K, as is standard practice, meaning they do not include thermal contributions such as vibrational entropy or zero-point energy. As such, they represent only the electronic (internal) energy of a perfect crystal. Additionally they do not account for impurities and structural disorder (as in case of form II). These simulations typically focus on potential energy without considering the entropic contributions that are critical to the melting process. As a result, the simplified models used in these calculations may not accurately reflect the complexities of real crystals, leading to discrepancies when comparing theoretical predictions with experimental fusion enthalpies. Slurry experiments were also carried out on crystals of both forms II

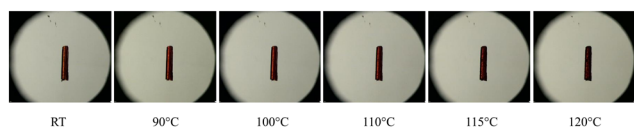


Fig. 7 HSM images showing the orange form I transforming to the red form II.



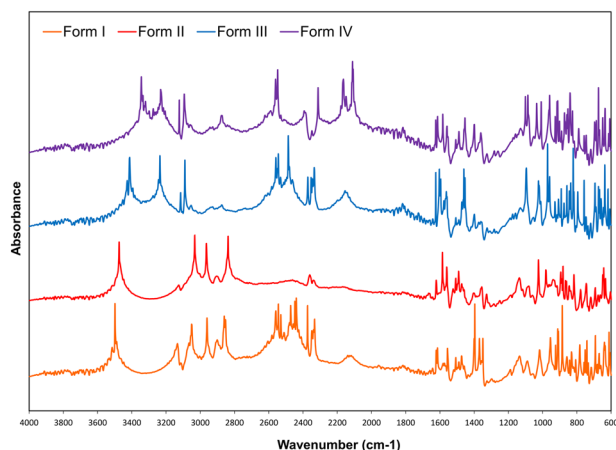


Fig. 8 Comparison of the reference infrared spectra of forms I, II, III, and IV. The fingerprint region allows for the clear differentiation of the different polymorphs.

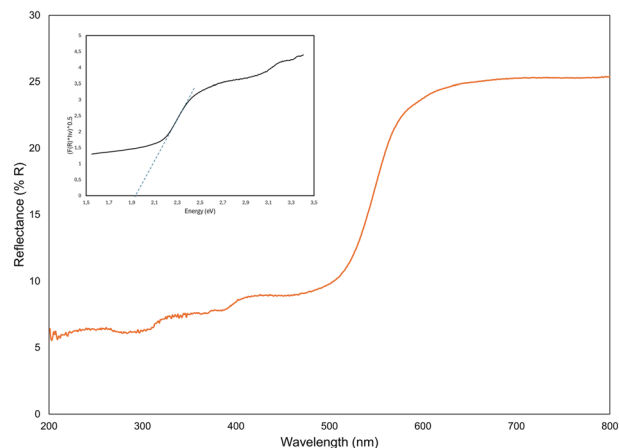


Fig. 9 Diffuse reflectance spectrum of form I with Tauc plot insert (see ESI† for forms II, III, and IV).

and **IV** since both do not show a phase transition before melting. Crystals of forms **II** and **IV** were placed together in a vial and dissolved in hexane to ascertain which form is the most thermodynamically stable of the two. After solvent evaporation, a red powder formed. A powder pattern was obtained, which matches the reference powder pattern of form **II** and thus confirms that form **II** is the most thermodynamically stable form (Fig. S12†). Samples of form **I** and form **III** were heated on the DSC until 130 °C and 170 °C respectively, then cooled back to 25 °C to determine whether their respective phase transitions are reversible or irreversible. Form **I** undergoes a reversible phase change, whilst form **III** undergoes an irreversible phase change (Fig. S14 and S15†). A powder pattern was then obtained for the sample of form **III**, after it underwent its phase transition in the DSC, and compared to the reference powder patterns of forms **II** and **IV**. It was found to be the most similar to form **II**, confirming that **III** converts irreversibly to **II** (Fig. S13†). Hot stage microscopy experiments of form **I** show a colour change from orange to red during the phase change (Fig. 7), thus indicating that the orange form **I** transforms to the red form **II**.

Infrared spectra of the four polymorphs were obtained (Fig. 8) since all four polymorphs are stable at room temperature. Assignments of the characteristic functional groups are given in Table 3. Form **II** has its N–H stretch at the highest wavenumber which suggests that form **II** possesses the strongest interaction of this type as supported by QTAIM analysis.

The optical band gaps of the four polymorphs were calculated from the DRS data using the Tauc plot method (Fig. 9).⁵² A direct bandgap was used based on the results of the modelling calculations. The results are presented in Table 4 together with electronic band structures and density of state (DOS) projected on all atomic orbitals in Fig. S22.†

Although the magnitudes differ, the trend is the same as for the bandgap values derived from periodic DFT calculations (largest value for form **III**, smallest value for form **II**, and values for **I**, **II** and **IV** are close to each other). The values also match up with the visual colour observed for the samples. Form **II** is a deep red in colour and form **III** has a clear orangey-yellow colour. It is noted that in the absence of detailed knowledge of the structure of the electronic energy levels near the band gap, the Tauc method only yields an approximate value for an optical band gap.

All the samples show a steady-state PL emission spectrum dominated by a broad band in the visible, centered around ~650 nm, using 380 nm excitation (Fig. 10). PL excitation measurements identified this as the optimum excitation wavelength. Form **III** clearly gives the most intense luminescence followed by forms **II**, **IV** and **I**. The PL emission spectra all occur in the red part of the spectrum, broadly overlapping with the range of values for the experimental optical bandgaps reported in Table 4. As a first approximation the emission peaks are likely to correspond to band-to-band emission processes. The PL curves are all similar in shape and position, indicating that the PL active electronic energy levels are similar and there are no significant differences in

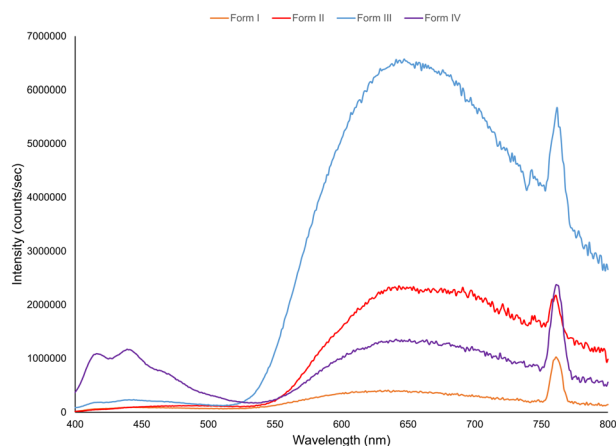
Table 3 Infrared spectral analysis

Assignment	Functional group	Wavenumber (cm ⁻¹)			
		Form I	Form II	Form III	Form IV
CO ₂ ⁻ asymmetric stretch	Carboxylate	1538 (s)	1542 (s)	1536 (s)	1538 (s)
CO ₂ ⁻ symmetric stretch	Carboxylate	1443 (m, br)	1433 (m, br)	1427 (m, br)	1431 (m, br)
N–H stretch	Pyridinium salt	3103 (m)	3114 (m)	3101 (m)	3111 (m)
O–H stretch	Phenol	3340 (s, br)	3295 (s, br)	3346 (s, br)	3283 (s, br)



Table 4 Experimental and theoretical band gap values obtained for the studied polymorphs

	Experimental/eV	Periodic DFT/eV
Form I	1.900	2.24
Form II	1.876	2.21
Form III	1.957	2.42
Form IV	1.912	2.23

**Fig. 10** Emission photoluminescence spectra of forms I, II, III, and IV acquired with 380 nm excitation wavelength. The sharp peak at 760 nm is the 2nd order peak of the excitation wavelength and should be ignored.

the electronic bonding of these states. It is acknowledged that low temperature PL data is likely required to study the emission processes in more detail.

Conclusions

Four polymorphs of the ternary molecular salt cocrystal complex (3-hydroxypyridinium)-(9-anthracenecarboxylate)-(trinitrobenzene) were successfully isolated. The ΔpK_a for the **9aca-3hp** acid-base pair is 1.3. Accordingly, this falls within the region of uncertainty around $\Delta pK_a = 1$, in the salt-cocrystal continuum, wherein the extent of proton transfer is unpredictable and the possibility of obtaining a salt or a cocrystal is very similar. In all four polymorphic forms proton transfer occurs from the carboxylic acid (**9aca**) to the pyridine (**3hp**) to form ternary molecular salts. Forms **I** and **III** undergo phase changes to forms **IV** and **II** respectively. From thermal analysis and slurry experiments, form **II** was found to be the most thermodynamically stable form. Red-orange-yellow colour polymorphism, shown by the four polymorphs, led to the study of their optical properties. Computational studies complemented these findings by providing a deeper understanding of the interactions and energetics underlying polymorphism. Lattice energy calculations confirmed the stability hierarchy of the polymorphs, with form **II** aligning well with experimental observations. Additionally, QTAIM and non-covalent interaction (NCI) analyses offered detailed insights into the nature and strength of hydrogen bonding and $\pi \cdots \pi$ interactions, underscoring their critical role in

self-assembly and stabilization. Notably, QTAIM highlighted subtle differences in bonding character that were not apparent from traditional force field methods, further advancing our understanding of these systems.

Band structure calculations and density of states analysis revealed a correlation between the electronic properties and the polymorphs' colours, emphasizing the impact of molecular arrangement on material properties. Quantum crystallography proved invaluable in dissecting the electron density distribution and interaction energies, offering a refined perspective on the interplay of structure and functionality.

In conclusion, this work integrates experimental and computational approaches to comprehensively characterize the polymorphism of the ternary molecular salt. The combined insights not only illuminated the intricate structure-property relationships but also demonstrated the potential of QCr as a powerful tool for advancing materials science, particularly in the design of functional materials with tuneable properties.

Data availability

The data supporting this article have been included as part of the ESI.† Crystallographic data for forms **I-IV** have been deposited in the CCDC with identification codes 2426460–2426463 respectively, and can be obtained from <https://www.ccdc.cam.ac.uk>.

Author contributions

All authors have given approval to the final version of the manuscript.

Conflicts of interest

There are no conflicts to declare.

Acknowledgements

AS would like to thank the NRF for their funding. The University of the Witwatersrand and the Molecular Sciences Institute are thanked for support and for providing the infrastructure required to do this work. Professor David G. Billing is thanked for use of the D2 diffractometer. AK gratefully acknowledges Polish high-performance computing infrastructure PLGrid (HPC Center: ACK Cyfronet AGH) for providing computer facilities and support within computational grant no. PLG/2023/016756.

References

- 1 S. Tothadi and G. R. Desiraju, *Chem. Commun.*, 2013, **49**, 7791–7793.
- 2 C. B. Aakeröy, N. Schultheiss, A. Rajbanshi, J. Desper and C. Moore, *Cryst. Growth Des.*, 2009, **9**, 432–441.
- 3 K. Kowalska, D. Trzybiński and A. Sikorski, *CrystEngComm*, 2015, **17**, 7199–7212.
- 4 P. Metrangolo and G. Resnati, *Chemistry*, 2001, **7**, 2511–2519.



- 5 F. Topić and K. Rissanen, *J. Am. Chem. Soc.*, 2016, **138**, 6610–6616.
- 6 C. C. Seaton, N. Blagden, T. Munshi and I. J. Scowen, *Chemistry*, 2013, **19**, 10663–10671.
- 7 T. Hill, D. C. Levendis and A. Lemmerer, *Acta Crystallogr., Sect. E: Crystallogr. Commun.*, 2018, **74**, 113–118.
- 8 C. Ortiz-de León and L. R. MacGillivray, *Chem. Commun.*, 2021, **57**, 3809–3811.
- 9 S. Chakraborty, L. Rajput and G. R. Desiraju, *Cryst. Growth Des.*, 2014, **14**, 2571–2577.
- 10 H. Jain, D. Sutradhar, S. Roy and G. R. Desiraju, *Angew. Chem., Int. Ed.*, 2021, **60**, 12841–12846.
- 11 R. Dubey, N. A. Mir and G. R. Desiraju, *IUCrJ*, 2016, **3**, 102–107.
- 12 N. A. Mir, R. Dubey and G. R. Desiraju, *IUCrJ*, 2016, **3**, 96–101.
- 13 S. Aitipamula, R. Banerjee, A. K. Bansal, K. Biradha, M. L. Cheney, A. R. Choudhury, G. R. Desiraju, A. G. Dikundwar, R. Dubey, N. Duggirala, P. P. Ghogale, S. Ghosh, P. K. Goswami, N. R. Goud, R. R. K. R. Jetti, P. Karpinski, P. Kaushik, D. Kumar, V. Kumar, B. Moulton, A. Mukherjee, G. Mukherjee, A. S. Myerson, V. Puri, A. Ramanan, T. Rajamannar, C. M. Reddy, N. Rodriguez-Hornedo, R. D. Rogers, T. N. G. Row, P. Sanphui, N. Shan, G. Shete, A. Singh, C. C. Sun, J. A. Swift, R. Thaimattam, T. S. Thakur, R. Kumar Thaper, S. P. Thomas, S. Tothadi, V. R. Vangala, N. Variankaval, P. Vishweshwar, D. R. Weyna and M. J. Zaworotko, *Cryst. Growth Des.*, 2012, **12**, 2147–2152.
- 14 F. Wöhler and J. Liebig, *Ann. Pharmacother.*, 1832, **3**, 249–282.
- 15 J. Thun, L. Seyfarth, C. Butterhof, J. Senker, R. E. Dinnebieer and J. Brey, *Cryst. Growth Des.*, 2009, **9**, 2435–2441.
- 16 A. J. Cruz-Cabeza, N. Feeder and R. J. Davey, *Commun. Chem.*, 2020, **3**, 142.
- 17 S. Tothadi, *CrystEngComm*, 2014, **16**, 7587–7597.
- 18 J. P. Smit and E. J. Hagen, *J. Chem. Crystallogr.*, 2015, **45**, 128–133.
- 19 C. Grossjohann, D. R. Serrano, K. J. Paluch, P. O'Connell, L. Vella-Zarb, P. Manesiotis, T. McCabe, L. Tajber, O. I. Corrigan and A. M. Healy, *J. Pharm. Sci.*, 2015, **104**, 1385–1398.
- 20 F. J. Acebedo-Martínez, C. Alarcón-Payer, A. Frontera, R. Barbas, R. Prohens, M. Di Crisci, A. Domínguez-Martín, J. Gómez-Morales and D. Choquesillo-Lazarte, *Pharmaceutics*, 2021, **13**, 2140.
- 21 A. O. Surov, K. V. Drozd, A. G. Ramazanov, A. V. Churakov, A. V. Vologzhanina, E. S. Kulikova and G. L. Perlovich, *Pharmaceutics*, 2023, **15**, 1747.
- 22 E. Sangtani, S. K. Sahu, S. H. Thorat, R. L. Gawade, K. K. Jha, P. Munshi and R. G. Gonnade, *Cryst. Growth Des.*, 2015, **15**, 5858–5872.
- 23 R. Sanii, Y. H. Andaloussi, E. Patyk-Kaźmierczak and M. J. Zaworotko, *Cryst. Growth Des.*, 2022, **22**, 3786–3794.
- 24 S. Aitipamula, I. Antonijevic, J. B. Baruah, O. B. Berryman, E. V. Boldyreva, D. A. Decato, M. Fourmigue, R. H. Groeneman, M. Gryl, K. M. Hutchins, K. Johmoto, A. Krawczuk, T. Leyssens, A. Manin, L. R. MacGillivray, D. Malenov, G. Perlovich, J. Stojakovic, A. Surov, R. B. H. Tan, J. H. Ter Horst, H. Uekusa and S. Zaric, *Multi-Component Crystals: Synthesis, Concepts, Function*, de Gruyter, 2018.
- 25 A. Lemmerer, *CrystEngComm*, 2020, **22**, 6091–6095.
- 26 B. A. Nogueira, C. Castiglioni and R. Fausto, *Commun. Chem.*, 2020, **3**, 34.
- 27 SAINT+, Version 6.0 (Includes XPREP and SADABS), Bruker AXS Inc, Madison, Wisconsin, USA, 2005.
- 28 L. Krause, R. Herbst-Irmer, G. M. Sheldrick and D. Stalke, *J. Appl. Crystallogr.*, 2015, **48**, 3–10.
- 29 G. M. Sheldrick, *Acta Crystallogr., Sect. C: Struct. Chem.*, 2015, **71**(Pt 1), 3–8.
- 30 L. Farrugia, *J. Appl. Crystallogr.*, 2012, **45**(4), 849–854.
- 31 A. Spek, *Acta Crystallogr., Sect. D: Biol. Crystallogr.*, 2009, **65**(2), 148–155.
- 32 C. F. Macrae, I. Sovago, S. J. Cottrell, P. T. A. Galek, P. McCabe, E. Pidcock, M. Platings, G. P. Shields, J. S. Stevens, M. Towler and P. A. Wood, *J. Appl. Crystallogr.*, 2020, **53**, 226–235.
- 33 A. Erba, J. K. Desmarais, S. Casassa, B. Civalleri, L. Donà, I. J. Bush, B. Searle, L. Maschio, L. Edith-Daga, A. Cossard, C. Ribaldone, E. Ascrizzi, N. L. Marana, J.-P. Flament and B. Kirtman, *J. Chem. Theory Comput.*, 2023, **19**, 6891–6932.
- 34 M. F. Peintinger, D. V. Oliveira and T. Bredow, *J. Comput. Chem.*, 2013, **34**, 451–459.
- 35 S. Grimme, J. Antony, S. Ehrlich and H. Krieg, *J. Chem. Phys.*, 2010, **132**, 154104.
- 36 H. J. Monkhorst and J. D. Pack, *Phys. Rev. B: Solid State*, 1976, **13**, 5188.
- 37 S. F. Boys and F. Bernardi, *Mol. Phys.*, 1970, **19**, 553–566.
- 38 Y. Hinuma, G. Pizzi, Y. Kumagai, F. Oba and I. Tanaka, *Comput. Mater. Sci.*, 2017, **128**, 140–184.
- 39 M. J. Frisch, G. W. Trucks, H. B. Schlegel, G. E. Scuseria, M. A. Robb, J. R. Cheeseman, G. Scalmani, V. Barone, G. A. Petersson, H. Nakatsuji, X. Li, M. Caricato, A. V. Marenich, J. Bloino, B. G. Janesko, R. Gomperts, B. Mennucci, H. P. Hratchian, J. V. Ortiz, A. F. Izmaylov, J. L. Sonnenberg, D. Williams-Young, F. Ding, F. Lipparini, F. Egidi, J. Goings, B. Peng, A. Petrone, T. Henderson, D. Ranasinghe, V. G. Zakrzewski, J. Gao, N. Rega, G. Zheng, W. Liang, M. Hada, M. Ehara, K. Toyota, R. Fukuda, J. Hasegawa, M. Ishida, T. Nakajima, Y. Honda, O. Kitao, H. Nakai, T. Vreven, K. Throssell, J. A. Montgomery Jr., J. E. Peralta, F. Ogliaro, M. J. Bearpark, J. J. Heyd, E. N. Brothers, K. N. Kudin, V. N. Staroverov, T. A. Keith, R. Kobayashi, J. Normand, K. Raghavachari, A. P. Rendell, J. C. Burant, S. S. Iyengar, J. Tomasi, M. Cossi, J. M. Millam, M. Klene, C. Adamo, R. Cammi, J. W. Ochterski, R. L. Martin, K. Morokuma, O. Farkas, J. B. Foresman and D. J. Fox, *Gaussian 16, Revision C.01*, Gaussian, Inc., Wallingford CT, 2016.
- 40 R. A. Boto, F. Peccati, R. Laplaza, C. Quan, A. Carbone, J. P. Piquemal, Y. Maday and J. Contreras-Garcia, *J. Chem. Theory Comput.*, 2020, **16**, 4150–4158.
- 41 J. Bernstein, R. E. Davis, L. Shimoni and N.-L. Chang, *Angew. Chem., Int. Ed. Engl.*, 1995, **34**, 1555–1573.
- 42 A. Gavezzotti, *Acc. Chem. Res.*, 1994, **27**, 309–314.
- 43 A. Gavezzotti, *Crystallogr. Rev.*, 1998, **7**, 5–121.



- 44 R. F. W. Bader, *Atoms in Molecules: A Quantum Theory*, Clarendon Press, 2003.
- 45 A. Krawczuk and A. Genoni, *Acta Crystallogr., Sect. B: Struct. Sci., Cryst. Eng. Mater.*, 2024, **80**, 249–274.
- 46 A. Genoni, L. Bučinský, N. Claiser, J. Contreras-García, B. Dittrich, P. M. Dominiak, E. Espinosa, C. Gatti, P. Giannozzi, J.-M. Gillet, D. Jayatilaka, P. Macchi, A. Ø. Madsen, L. Massa, C. F. Matta, K. M. Merz, P. N. H. Nakashima, H. Ott, U. Ryde, K. Schwarz, M. Sierka and S. Grabowsky, *Chem. – Eur. J.*, 2018, **24**, 10881–10905.
- 47 Y. A. Abramov, *Acta Crystallogr., Sect. A: Found. Crystallogr.*, 1997, **53**, 264–272.
- 48 D. Cremer and E. Kraka, *Angew. Chem., Int. Ed. Engl.*, 1984, **23**, 627.
- 49 E. Espinosa, I. Alkorta, J. Elguero and E. Molins, *J. Chem. Phys.*, 2002, **117**, 5529.
- 50 J. Contreras-García, E. R. Johnson, S. Keinan, R. Chaudret, J. P. Piquemal, D. N. Beratan and W. Yang, *J. Chem. Theory Comput.*, 2011, **7**, 625.
- 51 E. R. Johnson, S. Keinan, P. Mori-Sánchez, J. Contreras-García, A. J. Cohen and W. Yang, *J. Am. Chem. Soc.*, 2010, **132**, 6498.
- 52 P. Makuła, M. Pacia and W. Macyk, *J. Phys. Chem. Lett.*, 2018, **9**, 6814–6817.

